Rare Met. (2024) 43(1):186–197
https://doi.org/10.1007/s12598-023-02418-6

RARE METALS

ORIGINAL ARTICLE

Spatial construction of ultrasmall Pt-decorated 3D spinel oxide-modified N-doped graphene nanoarchitectures as high-efficiency methanol oxidation electrocatalysts

Qi Zhang, Min-Min Yan, Wen-Fa Du, Chen-Yu Yin, Jian Zhang, Lu Yang, Yun-Qing Kang, Hai-Yan He*, Hua-Jie Huang*

Received: 3 February 2023 / Revised: 18 March 2023 / Accepted: 4 April 2023 / Published online: 8 November 2023

Abstract Direct methanol fuel cell technology recently becomes the focus of both academic and engineering circles, which stimulates the exploitation and utilization of advanced electrode catalysts with high activity and long lifespan. Herein, we demonstrate a robust bottom-up approach to the spatial construction of three-dimensional (3D) spinel manganese-cobalt oxide-modified N-doped graphene nanoarchitectures decorated with ultrasmall Pt nanoparticles (Pt/$MnCo_2O_4$-NG) via a controllable self-assembly process. The incorporation of $MnCo_2O_4$ nanocrystals provides abundant hydroxyl sources to promote the oxidative removal of CO-like byproducts on Pt sites, while the existence of 3D porous N-doped graphene networks facilitates the transportation of both ions and electrons in the hybrid system, thus giving rise to remarkable synergetic coupling effects during the methanol oxidation process. Consequently, the optimized Pt/$MnCo_2O_4$-NG nanoarchitecture expresses exceptional electrocatalytic properties with a large electrochemically active surface area of 99.5 $m^2 \cdot g^{-1}$, a high mass activity of 1508.3 $mA \cdot mg^{-1}$, strong toxicity resistance and reliable long-term durability, which have obvious competitive advantages over those of conventional Pt/carbon black, Pt/carbon nanotube, Pt/graphene, and Pt/N-doped graphene catalysts with the same Pt usage.

Keywords Platinum; $MnCo_2O_4$; 3D graphene; Electrocatalysts; Methanol oxidation

1 Introduction

With the increasing threat of energy crisis and environmental pollution, the sustainable development of human society desperately needs to establish advanced energy-production and -consumption system [1–6]. Within this context, the design and usage of various green energy-generation and -conversion devices have been proved to be a critical way to achieve this objective [7–12]. As one of the most efficient and clean energy-conversion systems, fuel cells have become a hotspot of research in current academic and engineering circles [13–16]. Among diverse kinds of fuel cells, direct methanol fuel cell (DMFC) has shown great potential for a wide range of applications in aerospace, transportation, and portable electronics due to its unique advantages, such as high energy-transfer rate, low hazard emission, facile cell configuration, and fast start-up at room temperature [17, 18]. However, the sluggish methanol oxidation kinetics usually renders a dissatisfactory output power of DMFC, which requires the

Supplementary Information The online version contains supplementary material available at https://doi.org/10.1007/s12598-023-02418-6.

Q. Zhang, M.-M. Yan, W.-F. Du, C.-Y. Yin, L. Yang, H.-Y. He*, H.-J. Huang*
College of Mechanics and Materials, Hohai University, Nanjing 210098, China
e-mail: he.haiyan@hhu.edu.cn

H.-J. Huang
e-mail: huanghuajie@hhu.edu.cn

J. Zhang
New Energy Technology Engineering Lab of Jiangsu Province, College of Science, Nanjing University of Posts & Telecommunications (NUPT), Nanjing 210023, China

Y.-Q. Kang
International Center for Materials Nanoarchitectonics (WPI-MANA), National Institute for Materials Science, Tsukuba 305-0044, Ibaraki, Japan

exploitation and use of highly-active and long-life electrode catalysts to accelerate the anodic reaction [19, 20].

Currently, commercial anode catalysts of DMFC are mainly based on the platinum/carbon black (Pt/C) materials [21–23]. Because of the inherent microporous characteristics and inadequacy of surface growth sites for carbon black, it is difficult to ensure the uniform dispersion of Pt particles as well as restrain their sizes, thus resulting in an insufficient Pt utilization efficiency [24, 25]. In addition, it is known that Pt atoms with d-band structure are easily poisoned by the intermediate carbonaceous species (mainly CO), which largely shortens the working life of Pt-based catalysts and thus greatly hinders their large-scale industrial application [26, 27]. Hence, tremendous efforts have been made to explore alternative supports with optimized architectural design in order to liberate more exposed Pt sites and simultaneously strength the anti-toxicity ability [28–30].

In this aspect, graphene-based materials are catching considerable and persistent attention from a growing number of researchers [31, 32]. Specially, three-dimensional (3D) graphene aerogel constructed from two-dimensional (2D) graphene nanosheets has been regarded as an ideal matrix owing to its unique physicochemical properties, such as 3D pore-rich crosslinked networks, separated thin carbon layers, large specific surface area, and excellent electrical conductivity [33–35]. Nevertheless, it should be noted that pristine graphene nanosheets lack enough anchoring sites to immobilize Pt nanoparticles, which commonly induces the formation of large Pt clusters [36–38]. To circumvent this issue, nitrogen doping has been demonstrated to be an effective solution to optimize both the electronic structure and chemical activity of graphene, and meanwhile enhance its binding ability with Pt because of the ameliorative electron-donating character, thereby generating remarkable synergistic coupling effects during the electrocatalytic process [39, 40].

On the other hand, recent theoretical and experimental studies have testified that transition metal oxide (e.g., RuO_2, MnO_2, Co_3O_4) can serve as efficient catalytic promoters for methanol electrooxidation, which reduce the usage of metallic Pt and simultaneously create extra catalytically active sites [41, 42]. Compared with single transition metal oxides, spinel bimetal oxides commonly exhibit higher electrochemical activity owing to their structural flexibility and mixed valence states [43, 44]. Especially, spinel manganese-cobalt oxide ($MnCo_2O_4$) possesses a series of favorable textural features, including low cost, environmental friendliness, abundant active sites, and good chemical stability, thus holding great potential of application in the electrocatalysis field [45, 46]. Moreover, $MnCo_2O_4$ nanocrystals are also capable to offer a plenty of OH species in the catalytic system, which are very helpful to facilitate the oxidative removal of CO intermediates on Pt surface in the methanol oxidation process [47, 48]. Therefore, it is a feasible way to enhance the catalytic performance through the rational integration of Pt nanoparticles, $MnCo_2O_4$ nanocrystals, and N-doped graphene nanosheets into a 3D ternary nanoarchitecture. However, until now, the growth and assembling of small-sized Pt nanoparticles on $MnCo_2O_4$–modified N-doped graphene surface remains challenging in this area.

In this work, we propose a convenient and robust bottom-up strategy to the spatial construction of 3D $MnCo_2O_4$-modified N-doped graphene nanoarchitectures decorated with ultrasmall Pt nanoparticles (Pt/$MnCo_2O_4$-NG) via a controllable self-assembly process. Figures 1, S1 illustrate the overall synthesis process for the 3D Pt/$MnCo_2O_4$-NG nanoarchitectures, which mainly includes: (1) the fabrication of graphene oxide (GO) nanosheets by oxidation of natural graphite powder based on an improved Hummers' approach; (2) spatial construction of 3D interconnected porous N-doped graphene aerogel via a hydrothermal self-assembly reaction, followed by the modification of $MnCo_2O_4$ nanocrystals onto the N-doped graphene layers; (3) in-situ growth of Pt nanoparticles onto the surface of 3D $MnCo_2O_4$-NG hybrid aerogel in a water-ethylene glycol mixed medium. Such a 3D sophisticated architectural design not only effectively avoids the longitudinal stacking of graphene nanosheets, but also offers high-quality multidimensional platforms for the homogeneous deposition of Pt and $MnCo_2O_4$ nanoparticles, which are favorable for the fast transportation of reactants and exposure of active sites to boost the electrocatalytic efficiency. Consequently, the newly-developed Pt/$MnCo_2O_4$-NG catalysts exhibit superior methanol oxidation performance, significantly surpassing that of the conventional Pt/carbon black (Pt/C), Pt/carbon nanotube (Pt/CNT), Pt/graphene (Pt/G), and Pt/N-doped graphene (Pt/NG) catalysts with the identical testing condition.

2 Experimental

2.1 Synthesis of 3D Pt/$MnCo_2O_4$-NG nanoarchitectures

GO was firstly prepared from commercial graphite powders by an optimized Hummers' method [49]. The obtained GO nanosheets were then suspended in deionized water to achieve a concentration of 2 mg·ml^{-1}. The 3D Pt/$MnCo_2O_4$-NG nanoarchitectures with different $MnCo_2O_4$/NG ratios were constructed via this bottom-up synthetic method. Typically, taking the $MnCo_2O_4$/NG ratio of 2:1 as an example, the specific synthesis process is as follows: 5 ml GO dispersion (2 mg·ml^{-1}) was put into a reaction

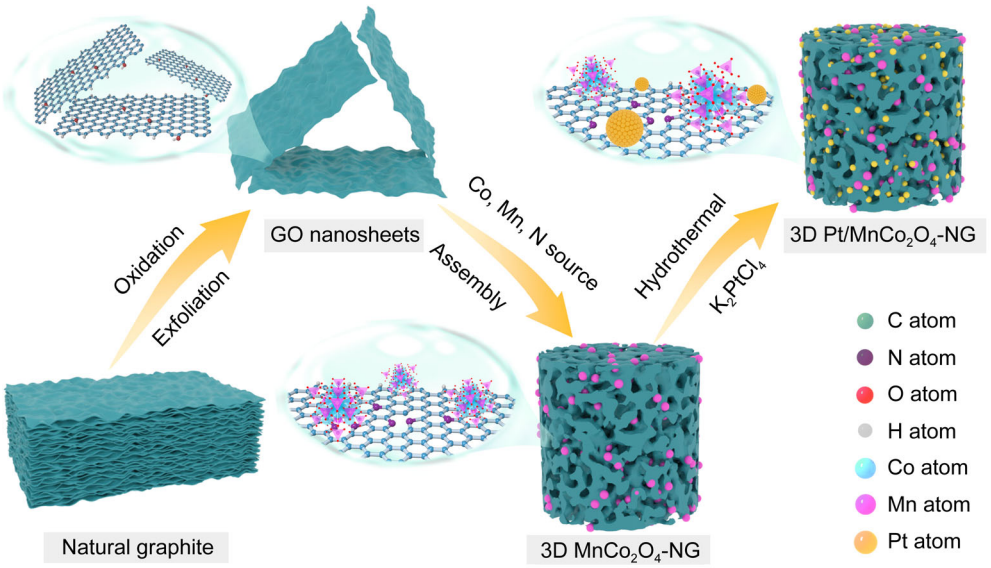

Fig.1 Overall synthesis process for 3D Pt/$MnCo_2O_4$-NG nanoarchitectures: (1) fabrication of GO nanosheets by oxidation of graphite powder; (2) construction of 3D N-doped graphene aerogel modified with $MnCo_2O_4$ nanocrystals; (3) in-situ growth of small-sized Pt onto surface of 3D $MnCo_2O_4$-NG aerogel

beaker, and then mixed with 0.28 ml $Co(Ac)_2$ solution (0.6 mol·L^{-1}), 0.14 ml $MnCl_2$ solution (0.6 mol·L^{-1}), and 30 ml water with magnetic stirring. Subsequently, 1 ml ammonia was introduced into the above solution in the fume hood, sealed and stirred continuously at 80 °C for 10 h. After that, the reacted solution was moved to a Teflon autoclave and reacted at 180 °C for 24 h. During the solvothermal reaction, the plentiful oxygen-containing groups on GO nanoflakes would interconnect to generate a 3D monolithic hydrogel [50, 51], while the N atoms could enter the carbon skeletons and meanwhile $MnCo_2O_4$ nanocrystals were immobilized on the doped graphene surface. In order to maintain the 3D porous structure of the sample and prevent graphene sheet from re-packing, the above hydrogel was converted into a $MnCo_2O_4$-NG aerogel by freeze-drying. Subsequently, the as-obtained 10 mg $MnCo_2O_4$-NG aerogel was placed in an ethylene glycol solution containing 0.128 ml K_2PtCl_4 (0.1 mol·L^{-1}, Alfa Aesar) and stirred for 15 min, and further heated at 120 °C for 12 h to form the desired Pt/$MnCo_2O_4$-NG hybrid. The components of the Pt/$MnCo_2O_4$-NG catalysts can be conveniently controlled by changing the feeding ratio of $MnCo_2O_4$ to NG during the above synthesis process. In this work, we used four different $MnCo_2O_4$/NG ratios, including 4:1, 2:1, 1:1 and 1:2, and the four prepared catalysts were abbreviated as Pt/$(MnCo_2O_4)_4$-$(NG)_1$, Pt/$(MnCo_2O_4)_2$-$(NG)_1$, Pt/$(MnCo_2O_4)_1$-$(NG)_1$, and Pt/$(MnCo_2O_4)_1$-$(NG)_2$, respectively. In addition, we also prepared the conventional carbon black (Vulcan XC-72R), carbon nanotube (CAS Chengdu Organic Chemistry Co., Ltd), graphene, and N-doped graphene supported Pt samples as reference catalysts by the similar synthesis steps except for the use of different supporting materials. The actual Pt, Mn, and Co contents in the Pt/$(MnCo_2O_4)_2$-$(NG)_1$ catalyst were measured as 18.6 wt%, 10.3 wt% and 25.7 wt% by inductively couples plasma mass spectrometer (ICP-MS), respectively, which are close to their theoretical contents.

2.2 Characterization

The 3D porous structure and micromorphology of the 3D porous Pt/$MnCo_2O_4$-NG nanoarchitectures were observed and analyzed using field-emission scanning electron microscopy (FESEM, Zeiss Sigma) and high-resolution transmission electron microscopy (HRTEM, JEOL JEM-2100F). The crystal structure, elemental composition and valence states of the Pt/$MnCo_2O_4$-NG nanostructure were investigated using powder X-ray diffraction (XRD, Bruker D8 Advance), Raman microscopy (Renishaw) and X-ray photoelectron spectroscopy (XPS, PHI Quantera with Al Kα radiation). The Micromeritics ASAP 2020 Plus system was employed to measure the specific surface area and porous properties of the Pt/$MnCo_2O_4$-NG nanoarchitectures. The detailed contents of various metallic species were tested by a PerkinElmer ELAN9000 ICP-MS.

2.3 Electrocatalytic measurements

A CHI 760E electrochemical workstation was used to investigate the electrocatalytic properties of the 3D Pt/$MnCo_2O_4$-NG nanoarchitectures towards the methanol

electrooxidation. The three-electrode testing system consists of a catalyst-coated glassy carbon (GC) disk as the working electrode, a Pt wire as the counter electrode, and a saturated calomel electrode as the reference electrode. To prepare the working electrode, the as-fabricated catalyst sample was put into an agate mortar and then subjected to a fine grinding to achieve a homogeneous silty state. 2 mg obtained fine powder was next dispersed in a mixed solution (475 μl water, 475 μl ethanol and 50 μl 5% Nafion 117 solution) by the mild sonication for 10 min. Afterwards, 5 μl catalyst suspension was transferred onto the GC surface and dried in air. Thus, the overall loading density of Pt on the GC electrode was kept at 0.028 mg·cm^{-2}.

The electrochemically active surface area (ECSA) value of the catalyst was estimated based on the H adsorption peak area by the following formula:

$$\mathrm{ECSA} = Q_{\mathrm{H}}/([\mathrm{Pt}] \times 0.21) \quad (1)$$

where [Pt] represents the platinum loading (g) on the electrode, Q_{H} is the charge for hydrogen adsorption (mC), and 0.21 represents the charge required to oxidize a monolayer of H_2 on bright Pt (mC·cm^{-2}). The mass activity (MA) of the catalyst for methanol electrooxidation was obtained with the use of the following formula:

$$\mathrm{MA} = I_{\mathrm{F}}/[\mathrm{Pt}] \quad (2)$$

where I_{F} is positive sweep peak current density of cyclic voltammetry curve (mA). Meanwhile, the specific activity (SA) was calculated through the following formula:

$$\mathrm{SA} = \mathrm{MA}/\mathrm{ECSA} \quad (3)$$

3 Results and discussion

The 3D porous characteristics and microscopic morphology of the Pt/$MnCo_2O_4$-NG nanoarchitecture were carefully studied by FESEM and TEM techniques. As presented in Fig. 2a, the representative FESEM image of Pt/$MnCo_2O_4$-NG clearly shows a well-defined 3D interconnected graphene network with continuously distributed macropores in the range from hundreds of nanometers to several microns. High-magnification FESEM observation reveals that a plenty of small-sized nanoparticles are closely attached to the N-doped graphene nanosheets without obvious agglomeration (Fig. 2b). TEM analysis further confirms that the ultrathin N-doped graphene sheets are decorated uniformly with both $MnCo_2O_4$ nanocrystals and Pt nanoparticles (Fig. 2c, d). According to the statistical data, the average particle diameter is estimated to be only ~ 3.8 nm, which is comparable to or even smaller

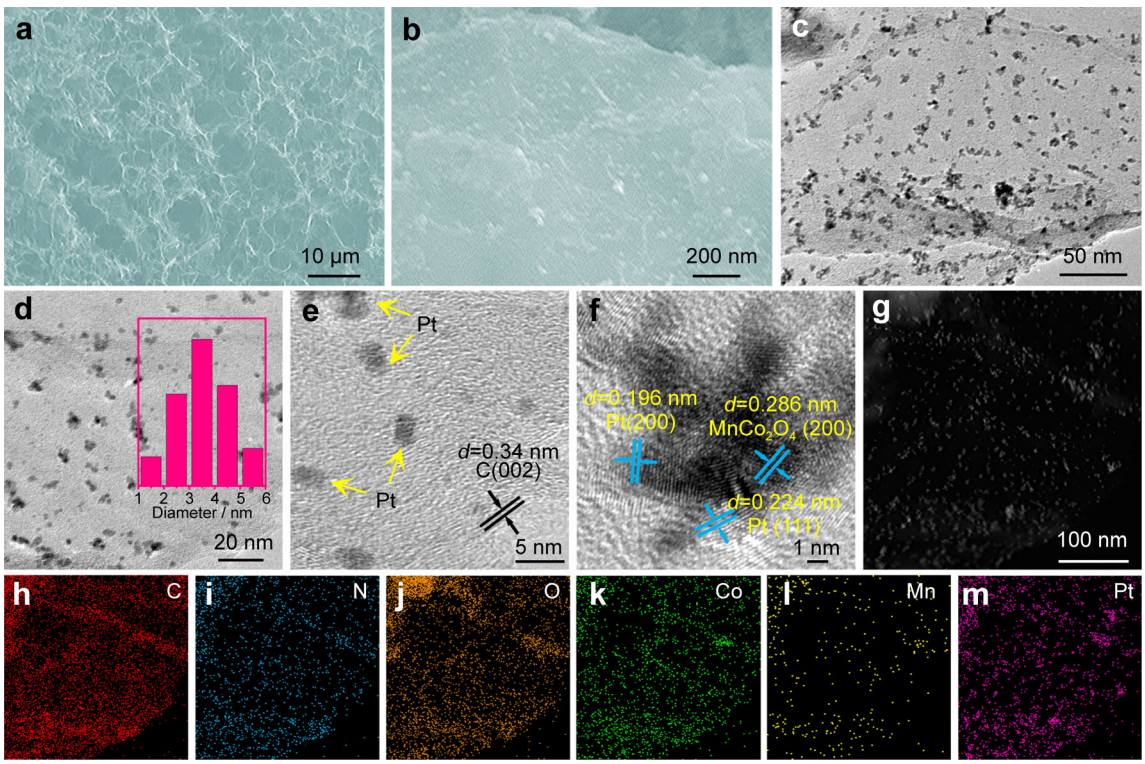

Fig. 2 Morphological analysis of 3D Pt/$MnCo_2O_4$-NG nanoarchitecture: typical **a**, **b** FESEM, **c**, **d** TEM and **e**, **f** HRTEM images showing a large number of ultrafine Pt nanoparticles grown on 3D $MnCo_2O_4$-NG network, and (inset in **d**) size distribution of Pt nanocrystals; **g** HAADF-STEM and elemental mapping images of **h** C, **i** N, **j** O, **k** Co, **l** Mn and **m** Pt

than that of previously reported nanocarbon-supported Pt catalysts [52, 53]. Taking into consideration that the sizes of $MnCo_2O_4$ nanocrystals are commonly larger than those of Pt nanoparticles [54, 55], the actual Pt average size for the Pt/$MnCo_2O_4$-NG nanoarchitecture should be even smaller than the above value. Furthermore, in order to clarify the compositions of these nanoparticles on N-doped graphene surface, we thoroughly analyzed the crystallographic textures with the assistance of HRTEM. Figure 2e, f discloses distinct lattice stripes with measured interplanar crystal spacings of 0.286, 0.224, and 0.196 nm, which correspond to the (220) crystal plane of spinel phase $MnCo_2O_4$, as well as the (111) and (200) crystal planes of Pt with face-centered cubic (fcc) structure, respectively, indicating that both Pt and $MnCo_2O_4$ nanoparticles have been successfully loaded onto the 3D N-doped graphene frameworks. Besides, the high-angle annular dark-field-scanning TEM (HAADF-TEM) and corresponding elemental mapping images confirm that the Pt/$MnCo_2O_4$-NG nanoarchitecture is composed of C, O, N, Co, Mn, and Pt, and all these six components are homogeneously distributed across the whole nanosheets (Fig. 2h–m).

The crystalline phase and chemical structure information of the Pt/$MnCo_2O_4$-NG nanoarchitecture was then analyzed by powder XRD and Raman spectroscopy. In Fig. 3a, the typical XRD pattern of GO shows an obvious carbon (002) diffraction peak at around $2\theta = 10.0°$, which is shifted to $2\theta = 24.5°$ in the Pt/G pattern, implying that the GO nanosheets have been reduced to graphene during the solvothermal self-assembled reaction. In sharp contrast, this carbon (002) characteristic peak almost disappears in the case of Pt/$MnCo_2O_4$-NG. This proves that the formation of 3D crosslinked graphene networks can well separate the neighbouring graphene nanolayers from each other to restrain their longitudinal stacking. In addition, a series characteristic peaks are found at $2\theta = 18.5°$ and 31.4°, corresponding to the (111) and (220) crystal planes of the tetragonal $MnCo_2O_4$ nanocrystals, respectively (JCPDS No. 23–1237). Meanwhile, other three prominent characteristic peaks at $2\theta = 39.8°$, 46.2°, and 67.5° are indexed to the (111), (200) and (220) planes of the cubic Pt structure, respectively (JCPDS No. 87–0646). Moreover, the average diameter of Pt nanoparticles in the Pt/$MnCo_2O_4$-NG catalyst is determined to be $\sim$ 3.5 nm based on the (200) plane

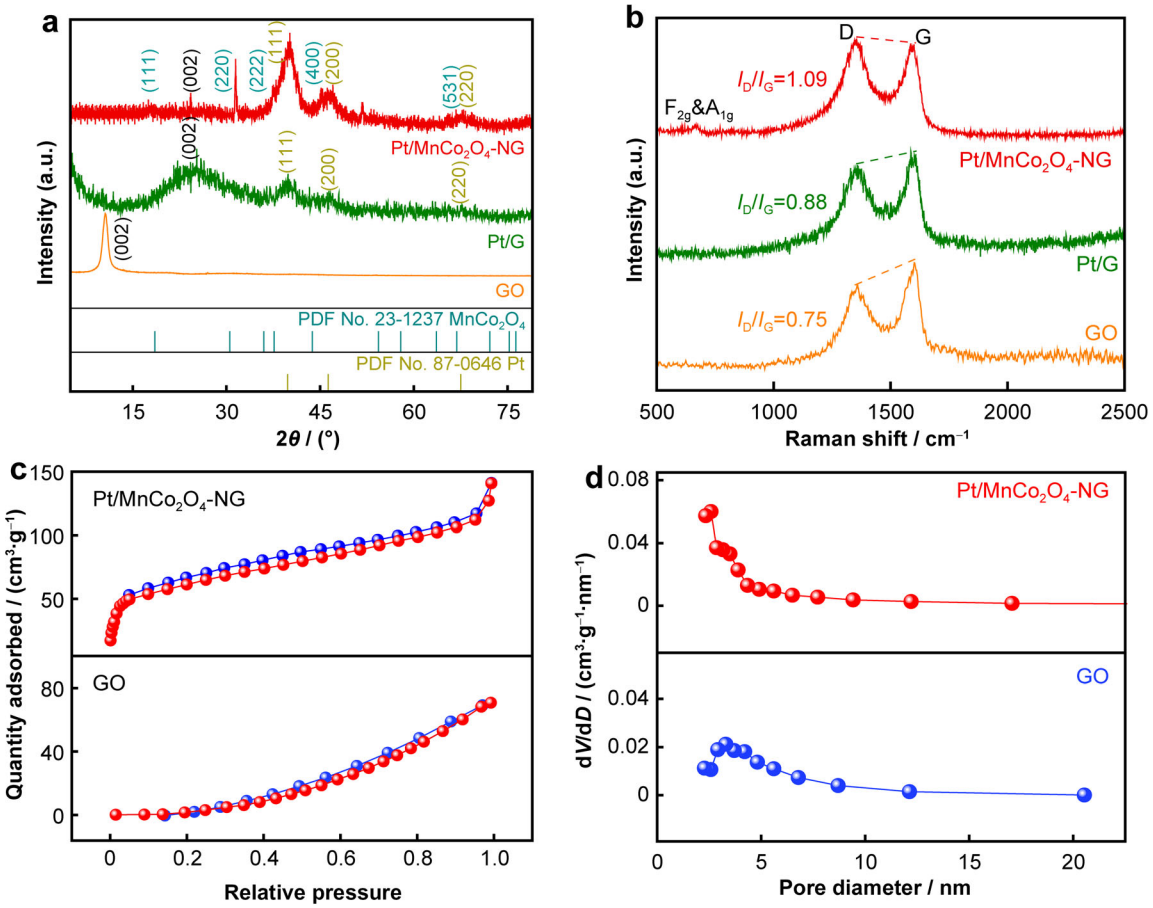

Fig. 3 Structural characterizations of Pt/$MnCo_2O_4$-NG nanoarchitecture: **a** XRD patterns and **b** Raman spectra of Pt/$MnCo_2O_4$-NG, Pt/G, and GO samples; **c** N_2 adsorption–desorption isotherms and **d** pore size distribution of Pt/$MnCo_2O_4$-NG and GO samples

through the Scherrer formula, which is slightly smaller than aforementioned TEM result. Figure 3b depicts the Raman spectra of the Pt/$MnCo_2O_4$-NG, Pt/G, and GO samples. Apparently, all these recorded spectra have two scattering signals centered at 1354 and 1595 cm^{-1}, belonging to the well-known D and G bands related to the disordered and ordered carbon atoms in graphitic carbon materials, respectively [56]. It is found that the D/G intensity ratio (I_D/I_G) of the Pt/$MnCo_2O_4$-NG material (1.09) is higher than that of Pt/G (0.88) and GO (0.75), which reflects an increased defect density induced by the incorporation of N atoms in the graphene skeleton. In addition, the characteristic A_{1g} signals of $MnCo_2O_4$ appearing at 660–670 cm^{-1} are also detected, suggesting the existence of $MnCo_2O_4$ nanocrystals on the N-doped graphene nanolayers [57]. Furthermore, the N_2 adsorption–desorption curve of the Pt/$MnCo_2O_4$-NG nanoarchitecture demonstrates its meso- and macroporous features with a Brunauer –Emmett –Teller (BET) surface area of up to 218.2 $m^2 \cdot g^{-1}$ (Fig. 3c, d), which is much larger than that of GO (11.2 $m^2 \cdot g^{-1}$) and close to that of previously-reported high-quality 3D graphene nanomaterials [50, 51].

XPS measurements were next performed to determine the elemental compositions and valence states of the Pt/$MnCo_2O_4$-NG nanoarchitecture. Figure 4a shows XPS survey spectrum of the Pt/$MnCo_2O_4$-NG nanoarchitecture, from which the C 1s, O 1s, N 1s, Co 2p, Mn 2p, and Pt 4f energy peaks were clearly observed, consistent with EDX result (Fig. S2). Moreover, the C 1s spectrum can be divided into four peaks at 284.7, 285.5, 286.3 and 288.5 eV (Fig. 4b), corresponding to the sp^2 C–C, C–N, C–OH and C=O groups, respectively. According to the integral peak areas, the proportion of oxygen containing groups for Pt/$MnCo_2O_4$-NG is much lower than that for GO (Fig. S3), indicative of the efficient reduction from GO to graphene. Meanwhile, the N 1s spectrum (Fig. 4c) consists of three energy peaks at 398.4, 400.0, and 401.8 eV, validating that there are three types of nitrogen species including pyridine N (N1), pyrrole N (N2) and graphite N (N3) in the Pt/$MnCo_2O_4$-NG catalyst, respectively. It has been proved that both N1 and N2 configurations have fixation effects for Pt nanoparticles, thus a large amount of N1 and N2 in Pt/$MnCo_2O_4$-NG plays a great role in maintaining the small sizes of Pt nanoparticles. Figure 4d shows complex Mn 2p spectrum of Pt/$MnCo_2O_4$-NG, which contains two pairs of double peaks: the two intensive peaks at 641.5 and 653.5 eV are due to Mn^{2+}, and the other cleavage peaks at 643.3 and 655.1 eV are ascribed to Mn^{3+} [55]. The

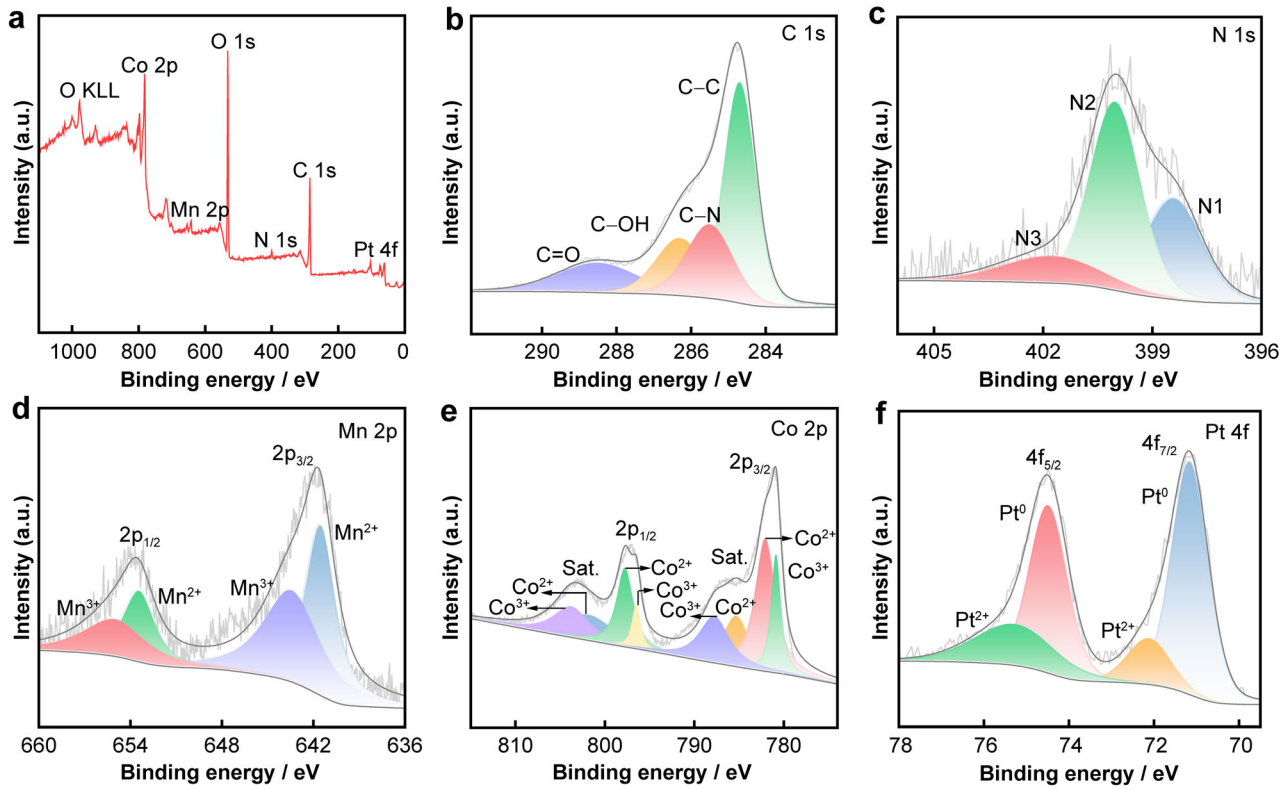

Fig. 4 XPS analysis of Pt/$MnCo_2O_4$-NG nanoarchitecture: **a** XPS survey spectrum showing presence of C, N, Mn, Co, O and Pt components; high-resolution **b** C 1s, **c** N 1s, **d** Mn 2p, **e** Co 2p and **f** Pt 4f spectra indicating co-existence metallic Pt, $MnCo_2O_4$ and N-doped graphene in hybrid nanostructure

deconvolution of Co 2p spectrum also generates Co^{2+} at 781.9, 785.3, 797.7 and 802.1 eV (Fig. 4e), while Co^{3+} at 780.7, 787.7, 796.5 and 803.8 eV, further attesting a mixture of multiple valence states [58]. Figure 4f shows the peak fitting of Pt 4f spectrum, where the intensive doublet at lower binding energies of 71.2 and 74.5 eV arise from metallic Pt, while the weak doublet at 72.1 and 75.3 eV are assigned to Pt^{2+}.

To make use of the intriguing architectural features, the Pt/$MnCo_2O_4$-NG nanoarchitectures were loaded on the surface of glassy carbon electrode and investigated their catalytic methanol oxidation performance under the acidic condition. First, the cyclic voltammetry (CV) curves of the Pt/$MnCo_2O_4$-NG catalysts with diverse $MnCo_2O_4$/NG ratios were recorded in 0.5 mol·L^{-1} H_2SO_4 solution. As shown in Fig. 5a, the typical hydrogen adsorption–desorption peaks are clearly observed in all CV curves of these four Pt/$MnCo_2O_4$-NG catalysts, which can be employed to assess their ECSAs. As calculated, the Pt/$(MnCo_2O_4)_2$-$(NG)_1$ catalyst is found to have the largest ECSA value of 99.5 m^2·g^{-1}, followed by the Pt/$(MnCo_2O_4)_1$-$(NG)_1$ (80.9 m^2·g^{-1}), Pt/$(MnCo_2O_4)_1$-$(NG)_2$ (69.0 m^2·g^{-1}), and Pt/$(MnCo_2O_4)_4$-$(NG)_1$ (66.7 m^2·g^{-1}). Notably, an optimal $MnCo_2O_4$/NG ratio (2:1) is not only capable to offer a large number of reachable active sites, but also to maintain a low charge transfer resistance in the catalytic system, thus giving full play to the synergistic effects. Meanwhile, the ECSA value of the selected Pt/$(MnCo_2O_4)_2$-$(NG)_1$ catalyst is 2.2, 3.1, 3.3 and 4.5 times larger than that of Pt/NG, Pt/G, Pt/CNT and Pt/C catalysts, respectively (Fig. 5b, c), which is attributed not only to the 3D crosslinked N-doped carbon networks, but also to the synergetic catalytic effects between $MnCo_2O_4$ nanocrystals and Pt nanoparticles. Moreover, the methanol oxidation mass activities of the Pt catalysts supported by different matrixes were then tested in a mixed solution of 0.5 mol·L^{-1} H_2SO_4 and 1 mol·L^{-1} CH_3OH by CV. As can be seen from Fig. 5d–f and Table S1, among the four catalysts with different $MnCo_2O_4$ loadings, the Pt/$(MnCo_2O_4)_2$-$(NG)_1$ catalyst possesses the highest methanol oxidation performance with an impressive mass activity value of up to 1508.3 mA·mg^{-1}, while the reference Pt/NG, Pt/G, Pt/CNT and Pt/C catalysts only have limited mass activities of 210.2–411.0 mA·mg^{-1}, which should be ascribed to their insufficient active sites or

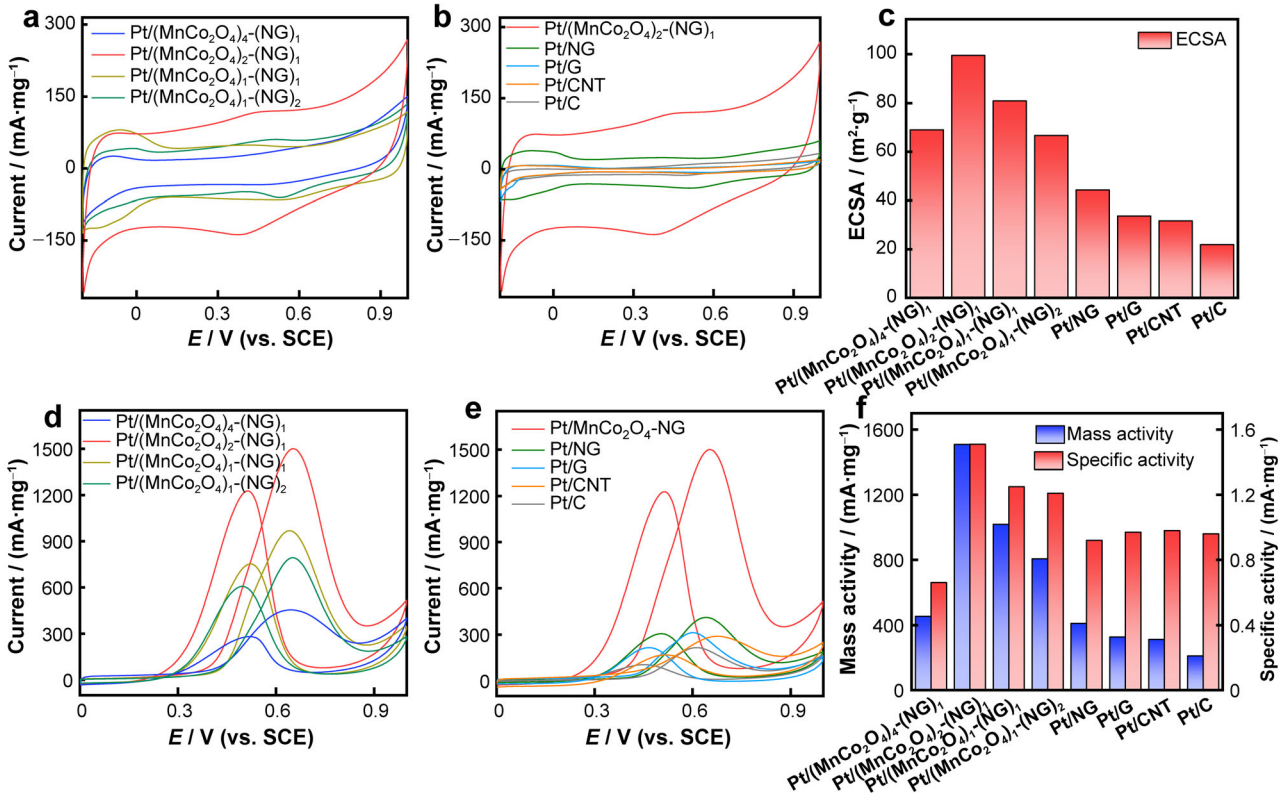

Fig. 5 Electrocatalytic performance of 3D Pt/$MnCo_2O_4$-NG catalysts for methanol electrooxidation: CV curves of **a** different Pt/$MnCo_2O_4$-NG electrodes and **b** Pt/$(MnCo_2O_4)_2$-$(NG)_1$, Pt/NG, Pt/G, Pt/CNT and Pt/C electrodes at 50 mV·s^{-1} in 0.5 mol·L^{-1} H_2SO_4 solution; **c** specific ECSA values for these studied electrodes; **d** CV curves of different Pt/$MnCo_2O_4$-NG electrodes and **e** Pt/$(MnCo_2O_4)_2$-$(NG)_1$, Pt/NG, Pt/G, Pt/CNT and Pt/C electrodes at 50 mV·s^{-1} in 0.5 mol·L^{-1} H_2SO_4 and 1 mol·L^{-1} CH_3OH mixture; **f** mass and specific activities of these studied electrodes

less porous nature. In addition, the ECSA-normalized specific activity of Pt/$(MnCo_2O_4)_2$-$(NG)_1$ (1.51 mA·cm^{-2}) manifests 26%–129% increments in comparison with the reference catalysts (Fig. S4), unraveling that the use of the $(MnCo_2O_4)_2$-$(NG)_1$ matrix can enhance the intrinsic catalytic activity of Pt component. Besides, as listed in Table S2, the overall methanol oxidation properties of the Pt/$(MnCo_2O_4)_2$-$(NG)_1$ catalyst are also superior to those of recent state-of-the-art Pt-based nanostructures, such as Pt/porous carbon [59, 60], Pt/modified CNTs [61, 62], Pt/heteroatom-doped graphene [63, 64], Pt-based nanodendrites [65, 66] and Pt-based nanowires [67, 68], further verifying the optimized Pt/$(MnCo_2O_4)_2$-$(NG)_1$ nanoarchitecture has extensive application prospect in the field of fuel cells.

To gain more insights into the electrocatalytic kinetics of the Pt/$(MnCo_2O_4)_2$-$(NG)_1$ and contrast catalysts, the linear sweep voltammetry (LSV) measurements and corresponding Tafel slope analysis were carried out. As displayed in Figs. 6a, S5, to derive a given methanol oxidation current, the Pt/$(MnCo_2O_4)_2$-$(NG)_1$ catalyst requires a remarkably lower electrode potential when compared with other catalysts, suggesting that the catalytic reaction is much easier to take place on the Pt/$(MnCo_2O_4)_2$-$(NG)_1$ electrode surface. Based on the above LSV data, the Tafel slope of the Pt/$(MnCo_2O_4)_2$-$(NG)_1$ catalyst is determined to be only 127 mV·dec^{-1}, which is obviously smaller than that of Pt/NG (164 mV·dec^{-1}), Pt/G (175 mV·dec^{-1}), Pt/CNT (261 mV·dec^{-1}) and Pt/C (217 mV·dec^{-1}) (Fig. 6b). This result convincingly testifies the use of the Pt/$(MnCo_2O_4)_2$-$(NG)_1$ catalyst can significantly speed up the electrocatalytic methanol oxidation kinetics, thereby achieving a much-improved Pt utilization efficiency.

The electrocatalytic durability is another essential performance indicator for the methanol oxidation catalyst, which plays a critical role in its commercialization process. To investigate the long-range stability of the Pt/$MnCo_2O_4$-NG catalyst, the current variation of the electrode at a given potential was investigated by using the chronoamperometry method. As clearly seen from Fig. 6c, at the early stage, the methanol oxidation currents on all electrodes are found to rapidly decrease with increasing the testing time, mainly due to the accumulation of CO-like byproducts on the Pt sites and the structural evolution of the catalysts. Afterwards, the current decay rate gradually drops and a pseudo-stable current platform is observed. Impressively, the Pt/$(MnCo_2O_4)_2$-$(NG)_1$ catalyst still retains a considerable oxidation current after 2000s, much better than the Pt/G, Pt/CNT and Pt/C catalysts. The distinctly improved poison tolerance and enhanced stability of

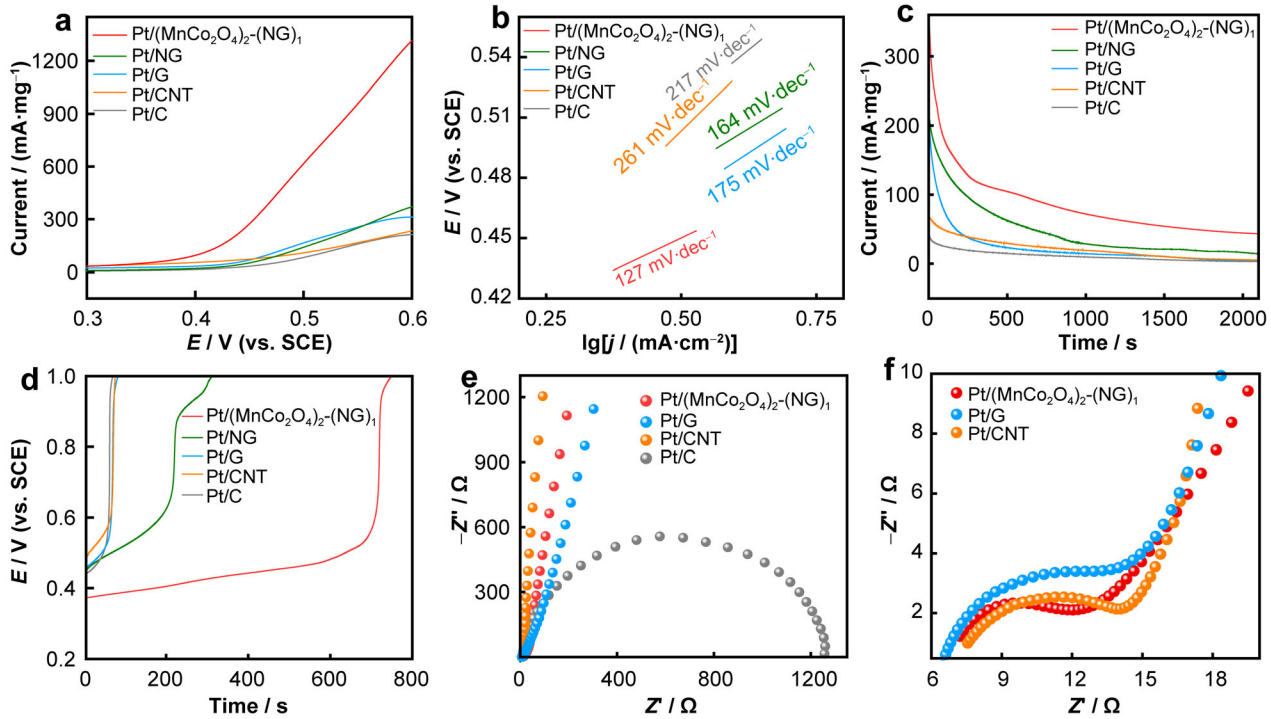

Fig. 6 **a** LSV curves, **b** Tafel plots, **c** chronoamperometric and **d** chronopotentiometry responses of Pt/$(MnCo_2O_4)_2$-$(NG)_1$, Pt/NG, Pt/G, Pt/CNT and Pt/C electrodes measured in 0.5 mol·L^{-1} H_2SO_4 and 1 mol·L^{-1} CH_3OH mixture, where current used for chronopotentiometric tests was acquired from forward scan of respective CV curve at 0.5 V; **e**, **f** AC impedance spectra of Pt/$(MnCo_2O_4)_2$-$(NG)_1$, Pt/G, Pt/CNT and Pt/C electrodes measured at their respective open circuit potential with an amplitude of 10 mV in 0.5 mol·L^{-1} H_2SO_4 and 1 mol·L^{-1} CH_3OH mixture

the Pt/$MnCo_2O_4$-NG catalyst should be linked to the following two reasons: on one hand, the introduction of $MnCo_2O_4$ nanocrystals offers a large number of hydroxyl sources to promote the oxidative elimination of CO on Pt sites; on the other hand, the large presence of N atoms in 3D graphene frameworks can immobilize Pt nanoparticles, which effectively prevents their agglomeration, dissolution, and Ostwald ripening phenomena.

Furthermore, chronopotentiometric tests were conducted to evaluate the anti-toxicity abilities of the Pt/$MnCo_2O_4$-NG and reference catalysts. As depicted in Fig. 6d, the anti-poisoning abilities of these catalysts are significantly different. Noticeably, the Pt/$(MnCo_2O_4)_2$-$(NG)_1$ electrode could last up to a maximum of 710 s at a low potential level, far outperforming the reference Pt/NG (220 s), Pt/G (65 s), Pt/CNT (60 s) and Pt/C (55 s) electrodes, which further demonstrates the high poison resistance of the Pt/$(MnCo_2O_4)_2$-$(NG)_1$ catalyst. Figure 6e, f presents the electrochemical alternating-current (AC) impedance spectra of various catalysts, where the high-frequency semicircle part can be employed to compare their electrical conductivity. According to the fitting results based on a standard equivalent circuit (Fig. S6), the charge transfer resistance (R_{ct}) value of the Pt/$(MnCo_2O_4)_2$-$(NG)_1$ catalyst is only 6.1 Ω, which is smaller than that of Pt/G (7.9 Ω), Pt/CNT (11.2 Ω), and Pt/C (1260.0 Ω) catalysts. The excellent electrical conductivity is expected to endow the Pt/$(MnCo_2O_4)_2$-$(NG)_1$ catalyst with abundant three-phase reaction boundaries, which enables fast electrochemical kinetics of the methanol oxidation reaction.

4 Conclusion

In summary, a facile and robust bottom-up method has been developed to the spatial construction of ultrasmall Pt-decorated 3D $MnCo_2O_4$-modified N-doped graphene nanoarchitectures through a controllable hydrothermal assembly reaction. Thanks to the 3D crosslinked porosity feature, high specific surface area, numerous N species, homogeneous Pt dispersion, and good electrical conductivity, the resulting Pt/$MnCo_2O_4$-NG catalyst with a proper $MnCo_2O_4$/NG ratio exhibits unusual electrocatalytic methanol oxidation performance with a large ECSA value of 99.5 $m^2 \cdot g^{-1}$, high mass/specific activity (1508.3 $mA \cdot mg^{-1}$/1.51 $mA \cdot cm^{-2}$), favorable poison tolerance, and excellent long-range stability, which are more competitive than the conventional Pt/C, Pt/CNT, Pt/G, and Pt/NG catalysts. We believe that such a design concept is also suitable for the bottom-up construction of other 3D graphene catalysts decorated with diverse spinel oxides (e.g., $CuCo_2O_4$, $CoFe_2O_4$, $NiCo_2O_4$) and noble metals (e.g., Pd, Au, Rh), which can serve as promising electrode materials for the next-generation fuel cell devices.

Acknowledgements This work was financially supported by the National Natural Science Foundation of China (Nos. 22209037 and 51802077) and the Fundamental Research Funds for the Central Universities (No. B220202042).

Declarations

Conflict of interests The authors declare that they have no conflict of interest.

References

[1] Hu Q, Gao KR, Wang XD, Zheng HJ, Cao JY, Mi LR, Huo QH, Yang HP, Liu JH, He CX. Subnanometric Ru clusters with upshifted D band center improve performance for alkaline hydrogen evolution reaction. Nat Commun. 2022;13(1):3958. https://doi.org/10.1038/s41467-022-31660-2.

[2] Xu XH, Zhang YJ, Miao XY. Synthesis and electrocatalytic performance of 3D coral-like NiCo-P. Chin J Rare Met. 2022;46(11):1449. https://doi.org/10.13373/j.cnki.cjrm.XY22080001.

[3] Huang HJ, Xue Y, Xie YS, Yang Y, Yang L, He HY, Jiang QG, Ying GB. MoS_2 quantum dot-decorated MXene nanosheets as efficient hydrogen evolution electrocatalysts. Inorg Chem Front. 2022;9(6):1171. https://doi.org/10.1039/d1qi01528a.

[4] Guo YM, Zhang LJ, XiLi D, Kang J. Advances of carbon materials as loaders for transition metal oxygen/sulfide anode materials. Chin J Rare Met. 2021;45(10):1241. https://doi.org/10.13373/j.cnki.cjrm.XY20040016.

[5] Shen BF, Feng Y, Wang Y, Sun PY, Yang L, Jiang QG, He HY, Huang HJ. Holey MXene nanosheets intimately coupled with ultrathin Ni–Fe layered double hydroxides for boosted hydrogen and oxygen evolution reactions. Carbon. 2023;212:118141. https://doi.org/10.1016/j.carbon.2023.118141.

[6] Zhang J, Zhou NN, Du M, Li YH, Cui Y, Li XA, Zhu XB, Huang W. Cobalt single-atom-decorated nickel thiophosphate nanosheets for overall water splitting. J Mater Chem A. 2022;10(1):296. https://doi.org/10.1039/d1ta08599a.

[7] Hu Q, Qin YJ, Wang XD, Wang ZY, Huang XW, Zheng HJ, Gao KR, Yang HP, Zhang PX, Shao MH, He CX. Reaction intermediate-mediated electrocatalyst synthesis favors specified facet and defect exposure for efficient nitrate–ammonia conversion. Energy Environ Sci. 2021;14(9):4989. https://doi.org/10.1039/d1ee01731d.

[8] Hu Q, Qin YJ, Wang XD, Zheng HJ, Gao KR, Yang HP, Zhang PX, Shao MH, He CX. Grain boundaries engineering of hollow copper nanoparticles enables highly efficient ammonia electrosynthesis from nitrate. CCS Chem. 2022;4(6):2053. https://doi.org/10.31635/ccschem.021.202101042.

[9] Jin X, Wang X, Liu YL, Kim MJ, Cao M, Xie HH, Liu ST, Wang XB, Huang W, Nanjundan AK, Yuliarto B, Li XY, Yamauchi Y. Nitrogen and sulfur co-doped hierarchically porous carbon nanotubes for fast potassium ion storage. Small. 2022;18(42):2203545. https://doi.org/10.1002/smll.202203545.

[10] Xu S, Niu M, Zhao GW, Ming SJ, Li XY, Zhu QL, Ding LX, Kim M, Alothman AA, Mushab MSS, Yamauchi Y. Size control and electronic manipulation of Ru catalyst over B, N co-doped carbon network for high-performance hydrogen evolution reaction. Nano Res. 2023;16:6212. https://doi.org/10.1007/s12274-022-5250-1.

[11] Ma C, He HY, Qin JL, Hao LL, Jia L, Yang L, Huang HJ. Combining MXene nanosheets with iron-based metal-organic

frameworks for enhanced electrocatalytic hydrogen evolution reaction. Mater Today Chem. 2023;30:101531. https://doi.org/10.1016/j.mtchem.2023.101531.
[12] Zhang J, Li LT, Du M, Cui Y, Li YH, Yan W, Huang HJ, Li XA, Zhu XB. Single-atom phosphorus defects decorated CoP cocatalyst boosts photocatalytic hydrogen generation performance of $Cd_{0.5}Zn_{0.5}S$ by directed separating the photogenerated carriers. Small. 2023;19(20):2300402. https://doi.org/10.1002/smll.202300402.
[13] Kim M, Firestein KL, Fernando JFS, Xu XT, Lim H, Golberg DV, Na J, Kim J, Nara H. Strategic design of Fe and N co-doped hierarchically porous carbon as superior ORR catalyst: from the perspective of nanoarchitectonics. Chem Sci. 2022;13(36):10836. https://doi.org/10.1039/d2sc02726g.
[14] Chen YZ, Zhou M, Huang YF, Ma YY, Yan LY, Zhou XW, Ma XZ, Zhao XL, Chen C, Bai J, Lin DH. Enhanced ethanol oxidation over Pd nanoparticles supported porous graphene-doped MXene using polystyrene particles as sacrificial templates. Rare Met. 2022;41(9):3170. https://doi.org/10.1007/s12598-022-02039-5.
[15] Ding QW, Luo Q, Lin L, Fu XP, Wang LS, Yue GH, Lin J, Xie QS, Peng DL. Facile synthesis of PdCu nanocluster-assembled granular films as highly efficient electrocatalysts for formic acid oxidation. Rare Met. 2022;41(8):2595. https://doi.org/10.1007/s12598-022-01997-0.
[16] Liu JB, Gong HS, Ye GL, Fei HL. Graphene oxide-derived single-atom catalysts for electrochemical energy conversion. Rare Met. 2022;41(5):1703. https://doi.org/10.1007/s12598-021-01904-z.
[17] Zhang Q, Li YA, He HY, Huang HJ. Building 3D interconnected MoS_2 nanosheet-graphene networks decorated with Rh nanoparticles for boosted methanol oxidation reaction. ACS Sustain Chem Eng. 2022;10(27):8940. https://doi.org/10.1021/acssuschemeng.2c02455.
[18] Xiao D, Jiang QG, Xu CY, Yang CZ, Yang L, He HY, Huang HJ. Interfacial engineering of worm-shaped palladium nanocrystals anchored on polyelectrolyte-modified MXene nanosheets for highly efficient methanol oxidation. J Colloid Interface Sci. 2022;616:781. https://doi.org/10.1016/j.jcis.2022.02.111.
[19] Qin JL, Huang HJ, Zhang J, Zhu FY, Luo L, Zhang C, Yang L, Jiang QG, He HY. Stereoassembly of ultrasmall Rh-decorated zeolite imidazolate framework-MXene heterostructures for boosted methanol oxidation reaction. J Mater Chem A. 2023;11(6):2848. https://doi.org/10.1039/d2ta08709j.
[20] Liu S, Wang X, Yu HG, Wu YP, Li B, Lan YQ, Wu T, Zhang J, Li DS. Two new pseudo-isomeric nickel (II) metal-organic frameworks with efficient electrocatalytic activity toward methanol oxidation. Rare Met. 2021;40(2):489. https://doi.org/10.1007/s12598-020-01596-x.
[21] Meng W, He HY, Yang L, Jiang QG, Yuliarto B, Yamauchi Y, Xu XT, Huang HJ. 1D–2D hybridization: nanoarchitectonics for grain boundary-rich platinum nanowires coupled with MXene nanosheets as efficient methanol oxidation electrocatalysts. Chem Eng J. 2022;450:137932. https://doi.org/10.1016/j.cej.2022.137932.
[22] Qin YC, Wang FQ, Wang XM, Wang MW, Zhang WL, An WK, Wang XP, Ren YL, Zheng X, Lv DC, Ahmad A. Noble metal-based high-entropy alloys as advanced electrocatalysts for energy conversion. Rare Met. 2021;40(9):2354. https://doi.org/10.1007/s12598-021-01780-7.
[23] Yang CZ, Jiang QG, Huang HJ, He HY, Yang L, Li WH. Polyelectrolyte-induced stereoassembly of grain boundary-enriched platinum nanoworms on $Ti_3C_2T_x$ MXene nanosheets for efficient methanol oxidation. ACS Appl Mater Interfaces. 2020;12(21):23822. https://doi.org/10.1021/acsami.0c02806.
[24] Huang HJ, Wang X. Recent progress on carbon-based support materials for electrocatalysts of direct methanol fuel cells. J Mater Chem A. 2014;2(18):6266. https://doi.org/10.1039/c3ta14754a.
[25] Gao ZQ, Li MM, Wang JY, Zhu JX, Zhao XM, Huang HJ, Zhang JF, Wu YP, Fu YS, Wang X. Pt nanocrystals grown on three-dimensional architectures made from graphene and MoS_2 nanosheets: highly efficient multifunctional electrocatalysts toward hydrogen evolution and methanol oxidation reactions. Carbon. 2018;139:369. https://doi.org/10.1016/j.carbon.2018.07.006.
[26] Yang CZ, Huang HJ, He HY, Yang L, Jiang QG, Li WH. Recent advances in MXene-based nanoarchitectures as electrode materials for future energy generation and conversion applications. Coord Chem Rev. 2021;435:213806. https://doi.org/10.1016/j.ccr.2021.213806.
[27] Guo XJ, Zhang Q, Li YN, Chen Y, Yang L, He HY, Xu XT, Huang HJ. Nanosized Rh grown on single-walled carbon nanohorns for efficient methanol oxidation reaction. Rare Met. 2022;41(6):2108. https://doi.org/10.1007/s12598-021-01882-2.
[28] Yang CZ, Jiang QG, Liu H, Yang L, He HY, Huang HJ, Li WH. Pt-on-Pd bimetallic nanodendrites stereoassembled on MXene nanosheets for use as high-efficiency electrocatalysts toward the methanol oxidation reaction. J Mater Chem A. 2021;9(27):15432. https://doi.org/10.1039/d1ta01784e.
[29] Dong AQ, Li H, Wu HM, Li KX, Shao YK, Li ZG, Sun SH, Wang WC, Hu WB. Weakening CO poisoning over size-and support-dependent Pt_n/X-graphene catalyst (X= C, B, N, n= 1–6, 13). Rare Met. 2023;42(3):1138. https://doi.org/10.1007/s12598-022-02210-y.
[30] Cao SY, Ye F, Zhang NN, Guo YL, Guo Y, Wang L, Dai S, Zhan WC. Synergistic effect of bimetallic RuPt/TiO_2 catalyst in methane combustion. Rare Met. 2023;42(1):165. https://doi.org/10.1007/s12598-022-02118-7.
[31] Huang HJ, Yan MM, Yang CZ, He HY, Jiang QG, Yang L, Lu ZY, Sun ZQ, Xu XT, Bando Y, Yamauchi Y. Graphene nanoarchitectonics: recent advances in graphene-based electrocatalysts for hydrogen evolution reaction. Adv Mater. 2019;31(48):1903415. https://doi.org/10.1002/adma.201903415.
[32] Huang H, Zhu J, Zhang W, Tiwary CS, Zhang J, Zhang X, Jiang Q, He H, Wu Y, Huang W, Ajayan PM, Yan Q. Controllable codoping of nitrogen and sulfur in graphene for highly efficient Li-oxygen batteries and direct methanol fuel cells. Chem Mater. 2016;28(6):1737. https://doi.org/10.1021/acs.chemmater.5b04654.
[33] He HY, Chen YX, Yang CZ, Yang L, Jiang QG, Huang HJ. Constructing 3D interweaved MXene/graphitic carbon nitride nanosheets/graphene nanoarchitectures for promoted electrocatalytic hydrogen evolution. J Energy Chem. 2022;67:483. https://doi.org/10.1016/j.jechem.2021.10.0192095-4956.
[34] Yang CZ, He HY, Jiang QG, Liu XY, Shah SP, Huang HJ, Li WH. Pd nanocrystals grown on MXene and reduced graphene oxide co-constructed three-dimensional nanoarchitectures for efficient formic acid oxidation reaction. Int J Hydrogen Energy. 2021;46(1):589. https://doi.org/10.1016/j.ijhydene.2020.09.243.
[35] Shen BF, Huang HJ, Jiang Y, Xue Y, He HY. 3D interweaving MXene-graphene network-confined Ni-Fe layered double hydroxide nanosheets for enhanced hydrogen evolution. Electrochim Acta. 2022;407:139913. https://doi.org/10.1016/j.electacta.2022.139913.
[36] Huang HJ, Wei YJ, Yang Y, Yan MM, He HY, Jiang QG, Yang XF, Zhu JX. Controllable synthesis of grain boundary-enriched Pt nanoworms decorated on graphitic carbon nanosheets for ultrahigh methanol oxidation catalytic activity. J Energy Chem. 2021;57:601. https://doi.org/10.1016/j.jechem.2020.08.063.
[37] Huang HJ, Ma LL, Tiwary CS, Jiang QG, Yin KB, Zhou W, Ajayan PM. Worm-shape Pt nanocrystals grown on

nitrogen-doped low-defect graphene sheets: highly efficient electrocatalysts for methanol oxidation reaction. Small. 2017;13(10):1603013. https://doi.org/10.1002/smll.201603013.
[38] Zhang X, Zhang JF, Huang HJ, Jiang QG, Wu YP. Platinum nanoparticles anchored on graphene oxide-dispersed pristine carbon nanotube supports: high-performance electrocatalysts toward methanol electrooxidation. Electrochim Acta. 2017;258:919. https://doi.org/10.1016/j.electacta.2017.11.142.
[39] Yan MM, Jiang QG, Zhang T, Wang JY, Yang L, Lu ZY, He HY, Fu YS, Wang X, Huang HJ. Three-dimensional low-defect carbon nanotube/nitrogen-doped graphene hybrid aerogel-supported Pt nanoparticles as efficient electrocatalysts toward the methanol oxidation reaction. J Mater Chem A. 2018;6(37):18165. https://doi.org/10.1039/c8ta05124k.
[40] Huang HJ, Guo XJ, Yan MM, Meng W, Xue Y, Xiao D, Jiang QG, Yang L, He HY. Well-dispersive Pt nanoparticles grown on 3D nitrogen- and sulfur-codoped graphene nanoribbon architectures: highly active electrocatalysts for methanol oxidation. Mater Today Energy. 2021;21:100814. https://doi.org/10.1016/j.mtener.2021.100814.
[41] Huang HJ, Zhu JX, Li DB, Shen C, Li MM, Zhang X, Jiang QG, Zhang JF, Wu YP. Pt nanoparticles grown on 3D RuO_2-modified graphene architectures for highly efficient methanol oxidation. J Mater Chem A. 2017;5(9):4560. https://doi.org/10.1039/c6ta10548c.
[42] Jiang ZY, Feng XB, Deng JL, He C, Douthwaite M, Yu YK, Liu J, Hao ZP, Zhao Z. Atomic-scale insights into the low-temperature oxidation of methanol over a single-atom Pt_1-Co_3O_4 catalyst. Adv Funct Mater. 2019;29(31):1902041. https://doi.org/10.1002/adfm.201902041.
[43] Zhang TW, Li ZF, Wang LK, Sun P, Zhang ZX, Wang SW. Spinel $MnCo_2O_4$ nanoparticles supported on three-dimensional graphene with enhanced mass transfer as an efficient electrocatalyst for the oxygen reduction reaction. Chemsuschem. 2018;11(16):2730. https://doi.org/10.1002/cssc.201801070.
[44] Kang Y, Zou D, Zhang JY, Liang F, Hayashi K, Wang H, Xue DF, Chen KF, Adair KR, Sun XL. Dual–phase spinel $MnCo_2O_4$ nanocrystals with nitrogen-doped reduced graphene oxide as potential catalyst for hybrid Na–air batteries. Electrochim Acta. 2017;11(16):2730. https://doi.org/10.1016/j.electacta.2017.05.100.
[45] Fu GT, Liu ZY, Zhang JF, Wu JY, Xu L, Sun DM, Zhang JB, Tang YW, Chen P. Spinel $MnCo_2O_4$ nanoparticles cross-linked with two-dimensional porous carbon nanosheets as a high-efficiency oxygen reduction electrocatalyst. Nano Res. 2016;9:2110. https://doi.org/10.1007/s12274-016-1101-2.
[46] Ma TY, Zheng Y, Dai S, Jaroniec M, Qiao SZ. Mesoporous $MnCo_2O_4$ with abundant oxygen vacancy defects as high-performance oxygen reduction catalysts. J Mater Chem A. 2014;2(23):8676. https://doi.org/10.1039/c4ta01672f.
[47] Wang NH, Xu ZH, Luo TT, Yan ZX, Jin M, Shi L. Pt anchored on $Mn(Co)CO_3$/$MnCo_2O_4$ heterostructure for complete oxidation of formaldehyde at room temperature. ChemistrySelect. 2020;5(34):10537. https://doi.org/10.1002/slct.202002870.
[48] Huang HJ, Shen BF, Yan MM, He HY, Yang L, Jiang QG, Ying GB. Coupled spinel manganese-cobalt oxide and MXene electrocatalysts towards efficient hydrogen evolution reaction. Fuel. 2022;328:125234. https://doi.org/10.1016/j.fuel.2022.125234.
[49] Kovtyukhova NI, Ollivier PJ, Martin BR, Mallouk TE, Chizhik SA, Buzaneva EV, Gorchinskiy AD. Layer-by-layer assembly of ultrathin composite films from micron-sized graphite oxide sheets and polycations. Chem Mater. 1999;11(3):771. https://doi.org/10.1021/cm981085u.
[50] Gong YJ, Yang SB, Liu Z, Ma LL, Vajtai R, Ajayan PM. Graphene-network-backboned architectures for high-performance lithium storage. Adv Mater. 2013;25(29):3979. https://doi.org/10.1002/adma.201301051.
[51] Wu ZS, Yang S, Sun Y, Parvez K, Feng X, Müllen K. 3D nitrogen-doped graphene aerogel-supported Fe_3O_4 nanoparticles as efficient electrocatalysts for the oxygen reduction reaction. J Am Chem Soc. 2012;134(22):9082. https://doi.org/10.1021/ja3030565.
[52] Maturost S, Themsirimongkon S, Waenkaew P, Promsawan N, Jakmunee J, Saipanya S. The effect of CuO on a Pt-Based catalyst for oxidation in a low-temperature fuel cell. Int J Hydrogen Energy. 2021;46(8):5999. https://doi.org/10.1016/j.ijhydene.2020.08.154.
[53] Daşdelen Z, Yıldız Y, Eriş S, Sen F. Enhanced electrocatalytic activity and durability of Pt nanoparticles decorated on GO-PVP hybride material for methanol oxidation reaction. Appl Catal B. 2017;219:511. https://doi.org/10.1016/j.apcatb.2021.120392.
[54] Liang YY, Wang HL, Zhou JG, Li YG, Wang J, Regier T, Dai HJ. Covalent hybrid of spinel manganese–cobalt oxide and graphene as advanced oxygen reduction electrocatalysts. J Am Chem Soc. 2012;134(7):3517. https://doi.org/10.1021/ja210924t.
[55] Fu W, Wang XL, Yang XX, He XQ. $MnCo_2O_4$ anchored on Nitrogen-doped carbon nanomaterials as an efficient electrocatalyst for oxygen reduction. ChemistrySelect. 2018;3(16):4228. https://doi.org/10.1002/slct.201703082.
[56] Guo XJ, Xiong J, Wang Q, Zhang J, He HY, Huang HJ. Ultrafine Rh nanocrystals grown onto a boron and nitrogen codoped carbon support with a horn-shaped structure for highly efficient methanol oxidation. Dalton Trans. 2022;51(44):16982. https://doi.org/10.1039/d2dt02010f.
[57] Ge XM, Liu YY, Goh FWT, Hor TSA, Zong Y, Xiao P, Zhang Z, Lim SH, Li B, Wang X, Liu ZL. Dual-phase spinel $MnCo_2O_4$ and spinel $MnCo_2O_4$/nanocarbon hybrids for electrocatalytic oxygen reduction and evolution. ACS Appl Mater Interfaces. 2014;6(15):12684. https://doi.org/10.1021/am502675c.
[58] Lu Y, Fan DQ, Chen ZP, Xiao WP, Cao CC, Yang XF. Anchoring Co_3O_4 nanoparticles on MXene for efficient electrocatalytic oxygen evolution. Sci Bull. 2020;65(6):460. https://doi.org/10.1016/j.scib.2019.12.020.
[59] Huang HJ, Yang SB, Vajtai R, Wang X, Ajayan PM. Pt-decorated 3D architectures built from graphene and graphitic carbon nitride nanosheets as efficient methanol oxidation catalysts. Adv Mater. 2014;26(30):5160. https://doi.org/10.1002/adma.201401877.
[60] Yang CZ, Jiang QG, Li WH, He HY, Yang L, Lu ZY, Huang HJ. Ultrafine Pt nanoparticle-decorated 3D hybrid architectures built from reduced graphene oxide and MXene nanosheets for methanol oxidation. Chem Mater. 2019;31(22):9277. https://doi.org/10.1021/acs.chemmater.9b02115.
[61] Guo SJ, Dong SJ, Wang EK. Constructing carbon nanotube/Pt nanoparticle hybrids using an imidazolium-salt-based ionic liquid as a linker. Adv Mater. 2010;22(11):1269. https://doi.org/10.1002/adma.200903379.
[62] Chu HB, Shen YH, Lin LA, Qin XJ, Feng G, Lin ZY, Wang JY, Liu HC, Li Y. Ionic-liquid-assisted preparation of Carbon nanotube-supported uniform noble metal nanoparticles and their enhanced catalytic performance. Adv Funct Mater. 2010;20(21):3747. https://doi.org/10.1002/adfm.201001240.
[63] Yuan X, Min YX, Wu JD, Xu L, Yue WB. Optimized electrocatalytic performance of PtZn intermetallic nanoparticles for methanol oxidation by designing catalyst support and fine-tuning surface composition. Electrochim Acta. 2021;394:139106. https://doi.org/10.1016/j.electacta.2021.139106.
[64] Huang HJ, Ye GL, Yang SB, Fei HL, Tiwary CS, Gong YJ, Vajtai R, Tour JM, Wang X, Ajayan PM. Nanosized Pt anchored onto 3D nitrogen-doped graphene nanoribbons towards efficient

methanol electrooxidation. J Mater Chem A. 2015;3(39):19696. https://doi.org/10.1039/c5ta05372b.
[65] Wang L, Nemoto Y, Yamauchi Y. Direct synthesis of spatially-controlled Pt-on-Pd bimetallic nanodendrites with superior electrocatalytic activity. J Am Chem Soc. 2011;133(25):9674. https://doi.org/10.1021/ja202655j.
[66] Guo SJ, Dong SJ, Wang EK. Three-dimensional Pt-on-Pd bimetallic nanodendrites supported on graphene nanosheet: facile synthesis and used as an advanced nanoelectrocatalyst for methanol oxidation. ACS Nano. 2010;4(1):547. https://doi.org/10.1021/nn9014483.
[67] Hong W, Wang J, Wang EK. Dendritic Au/Pt and Au/PtCu nanowires with enhanced electrocatalytic activity for methanol electrooxidation. Small. 2014;10(16):3262. https://doi.org/10.1002/smll.201400059.
[68] Guo SJ, Zhang S, Sun XL, Sun SH. Synthesis of ultrathin FePtPd nanowires and their use as catalysts for methanol oxidation reaction. J Am Chem Soc. 2011;133(39):15354. https://doi.org/10.1021/ja207308b.